

CT Reconstruction From Parallel and Fan-Beam Projections by a 2-D Discrete Radon Transform

Amir Averbuch, Ilya Sedelnikov, and Yoel Shkolnisky

Abstract—The discrete Radon transform (DRT) was defined by Averbuch *et al.* as an analog of the continuous Radon transform for discrete data. Both the DRT and its inverse are computable in $O(n^2 \log n)$ operations for images of size $n \times n$. In this paper, we demonstrate the applicability of the inverse DRT for the reconstruction of a 2-D object from its continuous projections. The DRT and its inverse are shown to model accurately the continuum as the number of samples increases. Numerical results for the reconstruction from parallel projections are presented. We also show that the inverse DRT can be used for reconstruction from fan-beam projections with equispaced detectors.

Index Terms—Computed tomography (CT), fan-beam projections, parallel projections, tomography, 2-D discrete Radon transform (DRT).

I. INTRODUCTION

TOMOGRAPHIC reconstruction underlies nearly all diagnostic imaging modalities, including X-ray computed tomography (CT), positron emission tomography, single-photon emission tomography, and certain acquisition methods for magnetic resonance imaging. It is also widely used for nondestructive evaluation in manufacturing and, more recently, for airport baggage security. Reconstruction in tomography means a recovery (inversion) from samples of either the X-ray transform (set of line-integral projections) or the Radon transform (set of integrals on planes) of an unknown object density distribution. In the 2-D case, they are the same.

In the 2-D case, the Radon transform of a function $f(x, y)$, denoted by $\mathfrak{R}f(\theta, s)$, is defined as the line integral of f along a line L inclined at angle θ and at distance s from the origin. Formally

$$\begin{aligned} \mathfrak{R}f(\theta, s) &= \int_L f(x, y) du \\ &= \int_{-\infty}^{\infty} \int_{-\infty}^{\infty} f(x, y) \delta(x \cos \theta + y \sin \theta - s) dx dy \end{aligned} \quad (1.1)$$

where $\delta(x)$ is Dirac's delta function [1], [3].

Manuscript received June 26, 2010; revised May 07, 2011; accepted July 27, 2011. Date of publication August 12, 2011; date of current version January 18, 2012. The associate editor coordinating the review of this manuscript and approving it for publication was Prof. Margaret Cheney.

A. Averbuch is with the School of Computer Science, Tel Aviv University, Tel Aviv 69978, Israel.

I. Sedelnikov is with Samsung Israel Research Center, Samsung Israel Research Center, Shoham 2, Ramat Gan, 52000, Israel.

Y. Shkolnisky is with the Department of Applied Mathematics, School of Mathematical Sciences, Tel Aviv University, Tel Aviv 69978, Israel.

Color versions of one or more of the figures in this paper are available online at <http://ieeexplore.ieee.org>.

Digital Object Identifier 10.1109/TIP.2011.2164416

In CT imaging, $f(x, y)$ is the distribution of the x -ray attenuation coefficient within the object. The goal of CT imaging is to reconstruct $f(x, y)$ from the projections of the object. Each projection is a collection of line integrals, as in (1.1). Parallel projection and fan-beam projection are two common acquisition geometries. Parallel projection is given by $\mathfrak{R}f(\theta, s)$ with fixed θ and varying s . Fan-beam projection is formed by line integrals along rays that emanate from a single source.

Due to physical constraints on the size and the number of detectors, in practice, each projection is comprised of a finite number of line integrals. For parallel projections, this means that $s \in \{s_1, \dots, s_m\}$ for some finite m . Only a finite number of projections can be collected, i.e., $\theta \in \{\theta_1, \dots, \theta_n\}$ for some integer n .

When a single source of radiation is used, fan-beam projections are more efficient since all the measurements in one fan are acquired simultaneously. For this reason, commercial CT scanners use fan-beam projections.

Computations speedups to recover objects from projections (either parallel or fan beam) are critical for next-generation real-time imaging systems. Several fast reconstruction algorithms have been proposed. Bresler *et al.* [7], [9] uses fast hierarchical algorithms for tomographic reconstruction where filtered back-projection (FBP) is the reconstruction method. The straightforward approach, which utilizes FBP, has a computational bottleneck of complexity $O(n^3)$ operations for a 2-D $n \times n$ image and at least $O(n^4)$ operations for a 3-D $n \times n \times n$ image. A family of fast hierarchical tomographic backprojection algorithms, which reduce the complexity to $O(n^2 \log n)$ for the 2-D case, was presented in [7] and [9]. The algorithm employs a divide-and-conquer strategy in the image domain and relies on the properties of harmonic decomposition of the Radon transform. For typical image sizes in medical applications or airport baggage security, these computations speed up by more than an order of magnitude. This algorithm is an accelerated version of the standard FBP reconstruction for parallel beam tomography. It provides orders of magnitude speedup in reconstruction time with little or no added distortion.

Other fast reconstruction algorithms, which exhibit $O(n^2 \log n)$ complexity, have been proposed. They include what is known collectively as Fourier reconstruction algorithms (FRAs) and multilevel inversion (MI) algorithms. FRAs are based on the Fourier slice theorem [2], which states that the Fourier transform of a projection at angle θ is a radial slice through the 2-D Fourier transform of the object at direction θ . Before the appearance of our algorithms [4], [5], on which the new algorithms in this paper are based, FRAs have been formed by the following sequence of steps:

- 1) a fast Fourier transform (FFT) is applied to the padded projections;

- 2) a 2-D Cartesian FFT grid is interpolated from the polar grid;
- 3) the image is recovered by a 2-D inverse FFT.

The difficulty lies in step 2. The interpolation step introduces distortions in the reconstruction since the Fourier transform is sensitive to these interpolations. The gridding method in [13] for the reconstruction was used in [7] for comparison with their performance.

According to [7], their algorithm outperforms the Fourier-based reconstruction algorithms [13] and the MI algorithm in [6]. Both have $O(n^2 \log n)$ complexity. The proposed hierarchical scheme has a superior cost versus distortion performance, as suggested in [7].

A model for finite Radon transforms that is composed of Radon projections is presented in [14]. They do not interpolate between points, but they perform summation over lines with “wraparound.” In some discretizations, “wraparound” is inherent, and this is a major drawback since algorithms, which are based on summation along wrapped lines, cannot be used for reconstruction from continuous projections (see Theorem II.2).

The proposed algorithms in this paper are simpler than those in [7]. In fact, they can be implemented using only 1-D FFTs. The underlying transforms for these algorithms are proven in [4] and [5] to be algebraically accurate, to preserve the geometric properties of the continuous transforms, and to be invertible and rapidly computable. In addition, it is shown in [5] that the discrete Radon transform (DRT) converges to the continuous Radon transform as the discretization step goes to zero. This property is of major theoretical and computational importance since it shows that the discrete transform indeed approximates the continuous transform; thus, it can be used to replace the continuous transform in digital implementations.

The equally sloped tomography (EST) method introduced in [10] is an iterative one, which allows reconstructions from a limited number of noisy projections [11], [12] through the use of total-variation regularization. The use of regularization also allows for the reduction of aliasing artifacts, which originated from incorrect sampling [e.g., inaccessible information beyond the resolution circle, (see [10] and [11])]. These works extend innovatively the pseudopolar representation [4], [5] on which we based our algorithm to overcome the problem of reconstruction from a limited number of noisy projections when, e.g., dose reduction is requested.

When the projection data, which were collected along the lines for which the discrete Radon transform is defined (where the distance between lines depends on the angle), is translated to the Fourier domain by means of a 1-D Fourier transform of each projection, the resulting data lie on the pseudopolar grid points and not on the polar grid. Therefore, the “resolution circle” problem does not exist due to the different acquisition geometry (the distance between lines depends on the acquisition angle). In this paper, multiple samples per detector width and a different acquisition geometry are described in Section IV, which together eliminate the resolution circle problem. Then, Radon transform reconstruction is preferable for two reasons: 1) As shown in Section III, correctly sampled projection reconstruction exhibits virtually no visible artifacts apart of a smoothing caused by the aperture function. In the situation when aliasing artifacts are not prominent, there is no added value in using the

EST regularization and 2) the inverse Radon transform is faster than the iterative procedure used in EST.

When the projection data contain aliased information (i.e., incorrectly sampled), the inverse Radon will exhibit reconstruction artifacts. In these cases, regularization used in EST has an advantage over formal inverse Radon since it reduces aliasing artifacts. When the collection procedure is designed such that the signal is band limited prior to sampling (aperture function) and the sampling rate is increased (multiple samples per detector width), then the severity of the aliasing problem decreases no matter if the “resolution circle” problem is present or not, due to the fact that the sampled signal becomes essentially band limited. The reconstruction examples presented in this paper are based on projections that satisfy both requirements.

The structure of this paper is as follows. Section II shortly describes the DRT [5] together with the results and properties that are relevant to the proposed algorithms. Section III demonstrates a reconstruction from samples of the continuous Radon transform, which is the basis for the reconstruction from fan-beam projections. Finally, in Section IV, we describe reconstruction from fan-beam projections, including the acquisition geometry and the “resorting” algorithm, which is the basis for the presented algorithm.

II. TWO-DIMENSIONAL DRT

A 2-D DRT is defined in [5] as an analog of the continuous Radon transform for discrete images.

Generally speaking, the DRT is defined by summing the discrete samples of an image $I(u, v)$ along lines with absolute slope less than 1. We define two families of lines: 1) a basically horizontal line is a line of the form $y = sx + t$, where $|s| \leq 1$, and 2) a basically vertical line is a line of the form $x = sy + t$, where $|s| \leq 1$.

For basically vertical lines, we traverse each line by unit horizontal steps $x = -n/2, \dots, n/2 - 1$, and for each x , we interpolate the image sample at position (x, y) by using trigonometric interpolation along the corresponding image column. For basically horizontal lines, we traverse the line by unit vertical steps, and for each integer y , we interpolate the value at the x -coordinate $x = s'y + t'$ by using trigonometric interpolation along the corresponding row. A formal definition of a 2-D Radon transform from [5] is provided in the following.

Definition II.1: 2-D Radon Transform for Discrete Images: Let $I(u, v)$, where $u, v = -n/2, \dots, n/2 - 1$, be an $n \times n$ array. Let s be a slope such that $|s| \leq 1$, and let t be an intercept such that $t = -n, \dots, n$. Then

$$\text{Radon}(\{y = sx + t\}, I) = \sum_{u=-n/2}^{n/2-1} \tilde{I}^1(u, su + t) \quad (2.1)$$

$$\text{Radon}(\{x = sy + t\}, I) = \sum_{v=-n/2}^{n/2-1} \tilde{I}^2(sv + t, v) \quad (2.2)$$

where for $u, v = -n/2, \dots, n/2 - 1, x, y \in \mathbb{R}$

$$\tilde{I}^1(u, y) = \sum_{v=-n/2}^{n/2-1} I(u, v) D_m(y - v) \quad (2.3)$$

$$\tilde{I}^2(x, v) = \sum_{u=-n/2}^{n/2-1} I(u, v) D_m(x - u) \quad (2.4)$$

$$D_m(t) = \frac{\sin(\pi t)}{m \sin(\pi t/m)}, \quad m = 2n + 1. \quad (2.5)$$

Moreover, for an arbitrary line l with slope s and intercept t , such that $|s| \leq 1$ and $t = -n, \dots, n$, the Radon transform is given by

$$(RI)(s, t) = \begin{cases} \text{Radon}(\{y = sx + t\}, I), & l \text{ is a basically} \\ & \text{horizontal line} \\ \text{Radon}(\{x = sy + t\}, I), & l \text{ is a basically} \\ & \text{vertical line.} \end{cases} \quad (2.6)$$

The 2-D discrete definition of the Radon transform is shown in [5] to be geometrically faithful as the lines used for the summation exhibit no “wraparound” effects. We also show that it satisfies a Fourier slice theorem, which states that the 1-D Fourier transform of the DRT is equal to the samples of the pseudopolar Fourier transform of the underlying image that lie along a ray.

There exists a special set of parallel projections for which the transform is rapidly computable and invertible. For a discrete image $I(u, v)$, where $u, v \in [-n/2 : n/2 - 1]$, this set consists of $n + 1$ basically horizontal and $n + 1$ basically vertical projections, i.e., given by the following sets:

$$S_H(t, l) = \left\{ y = \frac{2l}{n}x + t \right\} \text{ and } S_V(t, l) = \left\{ x = \frac{2l}{n}y + t \right\}$$

where $l \in [-n/2 : n/2]$ and $t \in [-n : n]$.

For a fixed $l \in [-n/2 : n/2]$, the l th basically horizontal projection is composed of summations along lines from the set $S_H(\cdot, l) = \{y = (2l/n)x + t | t \in [-n : n]\}$. The l th basically vertical projection is composed of summations along lines from the set $S_V(\cdot, l) = \{x = (2l/n)y + t | t \in [-n : n]\}$. We denote the results from these discrete summations by $P_H(t, l) = \text{Radon}(S_H(t, l), I)$ and $P_V(t, l) = \text{Radon}(S_V(t, l), I)$, where $l \in [-n/2 : n/2]$ and $t \in [-n : n]$.

The DRT [5] has both forward and inverse algorithms with complexity $O(n^2 \log n)$ for images of size $n \times n$. We briefly describe the inversion algorithms as they are the main ingredient of the proposed reconstruction procedure. There are two inversion approaches, i.e., an iterative and a direct. In both cases, we use the discrete version of the Fourier slice theorem [5] to transform the problem from the Radon domain into the Fourier domain, thus formulating the reconstruction problem as the inversion of a nonuniform Fourier transform on a certain nonuniform grid. The resulting frequency grid is the so-called pseudopolar grid [4].

The iterative algorithm is based on the application of the conjugate-gradient method to the Gram operator of the pseudopolar Fourier transform. Since both the forward pseudopolar Fourier transform and its adjoint can be computed in $O(n^2 \log n)$ operations, where $n \times n$ is the size of the input image, the Gram operator can also be computed in the same complexity. More specifically, both the pseudopolar Fourier transform and its adjoint can be computed using $100n^2 \log n$ operations plus small lower order terms [4]. This sums to $200n^2 \log n$ operations per

iteration. For comparison, the 2-D FFT of an $n \times n$ image requires $10n^2 \log n$ operations. The number of iterations is shown in [4] to be small for any practical image size (less than six iterations).

The advantage of the iterative inversion algorithm is its simplicity. On the other hand, it does not utilize the special frequency-domain structure of the transform, and its execution time depends on the specific image to invert. Thus, [4] provides also a direct inversion algorithm, which directly resamples the pseudopolar grid to a Cartesian frequency grid and then recovers the image from the Cartesian frequency grid. The algorithm is based on an “onion-peeling” procedure that, at each step, recovers two rows/columns of the Cartesian frequency grid, i.e., from the outermost rows/columns to the origin, by using columns/rows recovered in previous steps. The Cartesian samples of each row/column are recovered using trigonometric interpolation that is based on a fast multipole method. Finally, the original image is recovered from the Cartesian frequency samples, which are not the standard DFT samples, by using a fast Toeplitz solver. Full details on both algorithms are given in [4].

We prove in [5] that, if the image $I(u, v)$ consists of samples of a function $f(x, y)$ on a Cartesian grid, then the 2-D DRT of $I(u, v)$ approximates the continuous parallel projections of $f(x, y)$. Rephrasing the convergence theorem in [5], we have the following result.

Theorem II.2: Assume $f(x, y) \in Lip_\alpha(\mathbb{R})^1$ that equals to zero outside the square $(-1 + \varepsilon, 1 + \varepsilon) \times (-1 + \varepsilon, 1 - \varepsilon)$ for some $\varepsilon > 0$. Define $I_n(u, v) = f(u(2/n), v(2/n))$, where $n \in \mathbb{N}$. Then, for $n \rightarrow \infty$

$$\begin{aligned} & \left| \text{Radon} \left(\left\{ y = \frac{2l}{n}x + t \right\}, I_n \right) \right. \\ & \quad \left. \cdot \frac{2}{n} - \int_{-\infty}^{\infty} f \left(x, \frac{2l}{n}x + \frac{2t}{n} \right) dx \right| \longrightarrow 0 \\ & \left| \text{Radon} \left(\left\{ x = \frac{2l}{n}y + t \right\}, I_n \right) \right. \\ & \quad \left. \cdot \frac{2}{n} - \int_{-\infty}^{\infty} f \left(\frac{2l}{n}y + \frac{2t}{n}, y \right) dy \right| \longrightarrow 0 \end{aligned}$$

uniformly for $l \in [-n/2 : n/2]$ and $t \in [-n : n]$.

In order to establish a correspondence between the discrete projections and the samples of continuous projections, we define two families of line integrals as

$$L_H(\alpha, \beta) = \int_{-\infty}^{\infty} f(x, \alpha x + \beta) dx$$

and

$$L_V(\alpha, \beta) = \int_{-\infty}^{\infty} f(\alpha y + \beta, y) dy.$$

¹Lipschitz class $Lip_C(\alpha, \Omega)$: Let $\Omega \subseteq \mathbb{R}^n$. If $f : \mathbb{R}^n \rightarrow \mathbb{C}$ satisfies the condition $|f(x) - f(y)| \leq C \|x - y\|^\alpha$, where $0 < \alpha \leq 1$ for all $x, y \in \Omega$, then we say that f belongs to class $Lip_C(\alpha, \Omega)$. When the value of the constant C is not important, we say that f is Lipschitz α on Ω .

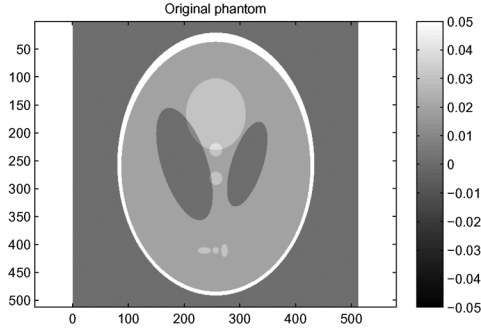


Fig. 1. Shepp-Logan head phantom.

For a fixed $\alpha \in [-1, 1]$, the function $L_H(\alpha, \beta)$, which is viewed as a function of β , is a continuous projection of $f(x, y)$ along the vector $(1, \alpha)$, where β is the intercept of the corresponding ray along the y -axis. For a fixed $\alpha \in [-1, 1]$, the function $L_V(\alpha, \beta)$, which is viewed as a function of β , is a continuous projection of $f(x, y)$ along the vector $(\alpha, 1)$, where β is the intercept of the corresponding ray along the x -axis.

By analogy with S_H and S_V in the discrete domain, we define two sets of lines in the continuous domain as follows:

$$\tilde{S}_H(t, l) = \left\{ y = \frac{2l}{n}x + \frac{2}{n}t \right\}$$

and

$$\tilde{S}_V(t, l) = \left\{ x = \frac{2l}{n}y + \frac{2}{n}t \right\}$$

where $l \in [-n/2 : n/2]$ and $t \in [-n : n]$.

We denote line integrals along these lines by

$$\tilde{P}_H(t, l) = L_H\left(\frac{2l}{n}, \frac{2t}{n}\right) \quad \text{and} \quad \tilde{P}_V(t, l) = L_V\left(\frac{2l}{n}, \frac{2t}{n}\right)$$

where $l \in [-n/2 : n/2]$ and $t \in [-n : n]$.

In fact, $\tilde{P}_H(t, l)$ is composed of sampled continuous parallel projections. Indeed, for a fixed l from $[-n/2 : n/2]$, the vector $\tilde{P}_H(t, l)$ consists of samples of the continuous projection $L_H((2l/n), \beta)$ at the points $2t/n$ for $t \in [-n : n]$. A similar statement is true for $\tilde{P}_V(t, l)$.

By Theorem II.2, $P_H(t, l) \cdot (2/n)$ converges to $\tilde{P}_H(t, l)$, and $P_V(t, l) \cdot (2/n)$ converges to $\tilde{P}_V(t, l)$ as n grows.

Theorem II.2 is illustrated by comparing between the discrete and the sampled continuous projections of the Shepp-Logan head phantom. The density function $f(x, y)$ of the Shepp-Logan phantom is a sum of indicator functions of ellipses weighted by the density of each ellipse. The function $f(x, y)$ equals zero outside the square $[-1, 1] \times [-1, 1]$. The advantage of the Shepp-Logan phantom is that an analytic expression for its projections can be derived. The full range of densities in the Shepp-Logan phantom is $[0, 1]$, which is equivalent to the range of $[0, 1000]$ in Hounsfield units (HU). The Shepp-Logan head phantom is displayed in Fig. 1 with a window width of 100 HU centered about water.

Notice that the Shepp-Logan phantom is not a Lipschitz function. Therefore, it violates the conditions of Theorem II.2.

TABLE I
RELATIVE l_2 ERROR BETWEEN THE ANALYTIC COMPUTATION AND THE APPROXIMATED PROJECTIONS

n	64	128	256	512	1024
Error	0.1803	0.0892	0.0461	0.0223	0.0117

Nonetheless, the discrete projections of the phantom closely approximate the continuous ones, as we will see in the following.

Consider the discrete image $I(u, v) = f(u(2/n), v(2/n))$, where $u, v \in [-n/2 : n/2 - 1]$, for some positive integer n . We compute the 2-D DRT for this image, which results in the two projections arrays P_H and P_V . We multiply both arrays by $2/n$ to approximate the sampled continuous projections. The scaled arrays for case $n = 512$ are displayed in Fig. 2(a).

We then compute the two arrays \tilde{P}_H and \tilde{P}_V of sampled continuous projections of $f(x, y)$ (see Fig. 2(b) for illustration). It follows from Theorem II.2 that the entries in P_H and P_V approximate the entries in \tilde{P}_H and \tilde{P}_V . In our example, the computed relative l_2 error between the arrays in Fig. 2(a) and (b) equals 0.0223. The absolute error is shown in Fig. 2(c).

Table I shows the relative l_2 errors between the samples of the analytic computation and the approximated projections of the Shepp-Logan phantom for different values of n .

We observe that, in the case of the Shepp-Logan phantom, the relative l_2 error is proportional to $1/n$.

Another way to estimate the quality of the approximations is to compute the relative l_2 error separately for each projection. Fig. 3 displays the graphs of the error as a function of the projection index $l \in [-n/2 : n/2]$ for $n = 512$.

The convergence of the discrete projections to sampled continuous projections implies that we can reconstruct $f(x, y)$ from its continuous projections by applying the 2-D inverse DRT.

III. RECONSTRUCTION FROM PARALLEL CONTINUOUS PROJECTIONS

In this section, we provide numerical evidence that the inverse DRT can be used for reconstruction from sampled X-ray projections.

The numerical examples are based on analytically computed parallel projections of the Shepp-Logan phantom.

Let $f(x, y)$ denote the continuous Shepp-Logan phantom, and let n be a fixed integer number. The arrays $\tilde{P}_H(t, l)$ and $\tilde{P}_V(t, l)$, which were defined in Section II, are composed from samples of the analytic projections of the Shepp-Logan phantom. We apply the 2-D inverse Radon transform to $\tilde{P}_H(t, l) \cdot (n/2)$ and to $\tilde{P}_V(t, l) \cdot (n/2)$, obtaining an $n \times n$ image, which approximates the original phantom $f(x, y)$ sampled at the points $\{(u(2/n), v(2/n)) | u, v \in [-n/2 : n/2 - 1]\}$.

However, since the analytic projections of the Shepp-Logan phantom are not bandlimited, the resulting image will suffer from aliasing artifacts. We provide an example of such reconstruction for $n = 512$ in Fig. 4(a). The reconstructed image is displayed using a window width of 100 HU that is centered around water. The difference between the samples of the Shepp-Logan phantom and the reconstructed image is displayed in Fig. 4(b) using a window width of 50 HU.

In practice, X-ray projections are always bandlimited due to the nonzero size of the detector aperture. We simulate the

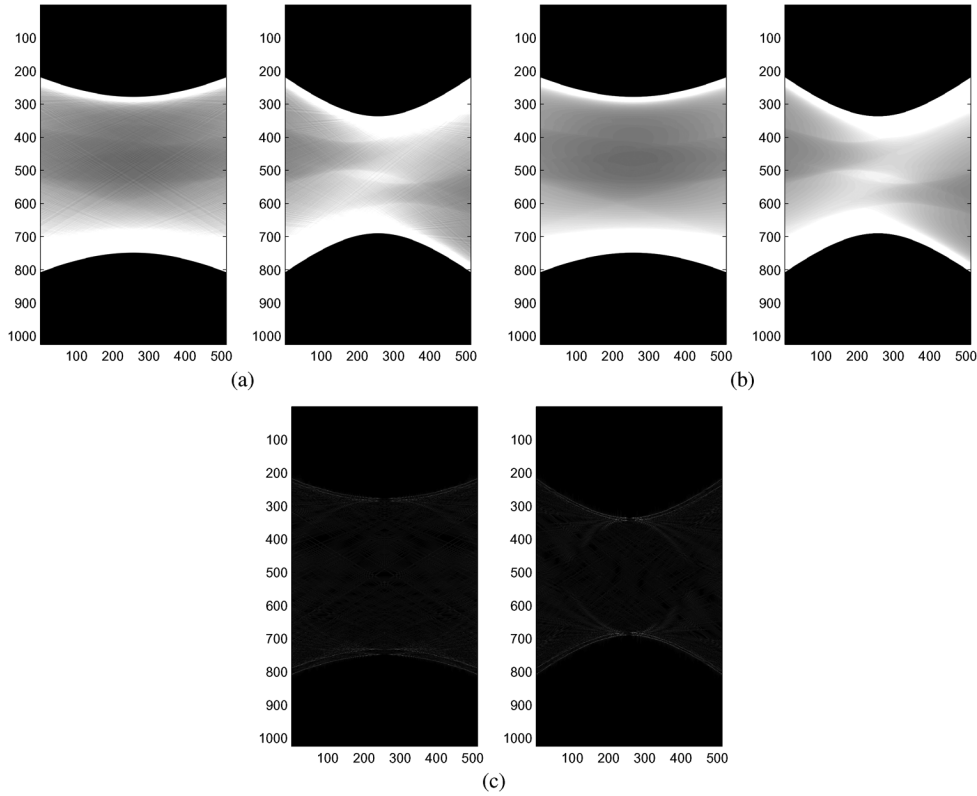


Fig. 2. Discrete projections versus continuous projections. (a) P_H and P_V . (b) \tilde{P}_H and \tilde{P}_V . (c) Absolute error.

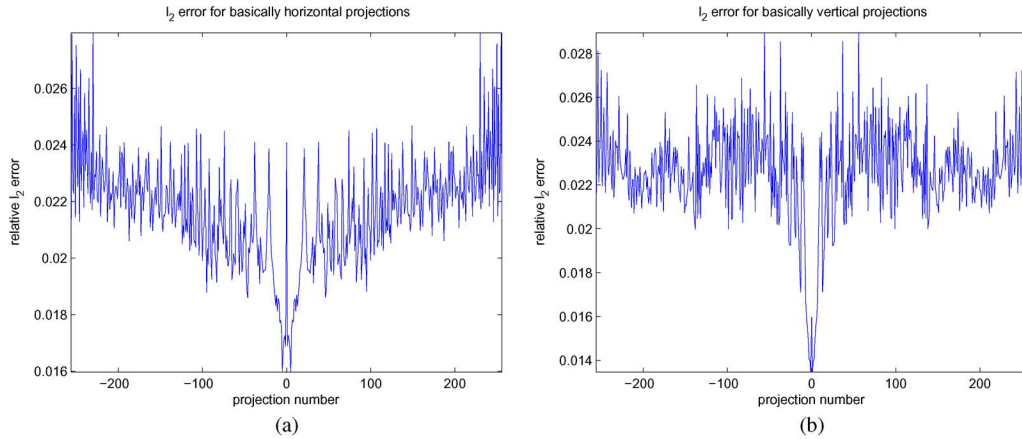


Fig. 3. Relative l_2 error as a function of the projection number l . (a) Basically horizontal. (b) Basically vertical.

nonzero detector aperture by convolving the analytic projections with an aperture function prior to sampling. We define

$$L_H^\sigma(\alpha, \beta) = L_H(\alpha, \beta) * \Pi_\sigma(\beta)$$

and

$$L_V^\sigma(\alpha, \beta) = L_V(\alpha, \beta) * \Pi_\sigma(\beta)$$

where the sensor aperture is simulated using convolution with a rectangular function, i.e.,

$$\Pi_\sigma(\beta) = \begin{cases} \frac{1}{2\sigma}, & \beta \in \{-\sigma, \sigma\} \\ 0, & \text{otherwise.} \end{cases} \quad (3.1)$$

σ should satisfy $\sigma \geq T_s$ in order to reduce aliasing, where T_s is a center-to-center distance between sensors (see [3, p. 188]).

This inequality means that there should be at least two samples per detector width. There exist a number of ways to measure multiple samples per detector width in practice (see [3, pp. 188–189]). In our simulation, $T_s = 2/n$, which is the distance between subsequent samples on the receiver line.

We sample the continuous projections convolved with the aperture function to obtain the following:

$$\tilde{P}_H^\sigma(t, l) = L_H^\sigma\left(\frac{2l}{n}, \frac{2t}{n}\right) \quad \text{and} \quad \tilde{P}_V^\sigma(t, l) = L_V^\sigma\left(\frac{2l}{n}, \frac{2t}{n}\right)$$

where $l \in [-n/2 : n/2]$ and $t \in [-n : n]$. We then apply the 2-D inverse Radon transform to $\tilde{P}_H^\sigma(t, l) \cdot (n/2)$ and $\tilde{P}_V^\sigma(t, l) \cdot (n/2)$ in order to obtain an $n \times n$ image, which approximates the original phantom $f(x, y)$ that is sampled at the points $\{(u(2/n), v(2/n)) | u, v \in [-n/2 : n/2 - 1]\}$. The resulting reconstruction for $n = 512$ and $\sigma = 2/n$ is

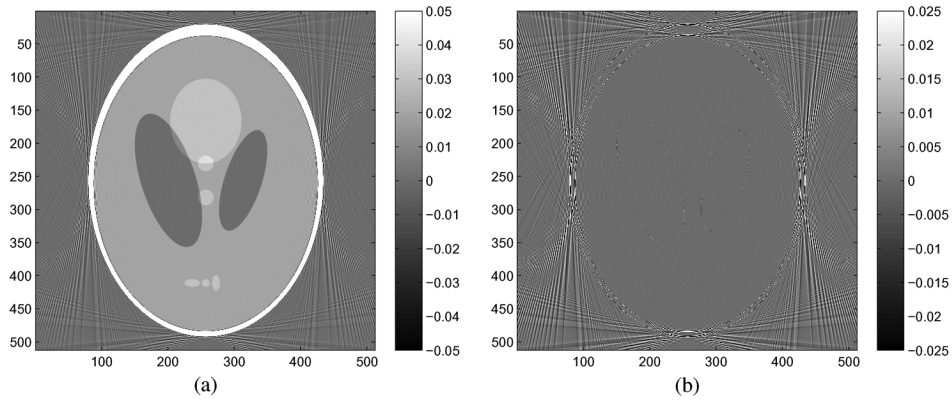


Fig. 4. Reconstruction from \tilde{P}_H and \tilde{P}_V . (a) Recovered Shepp-Logan. (b) Reconstruction error.

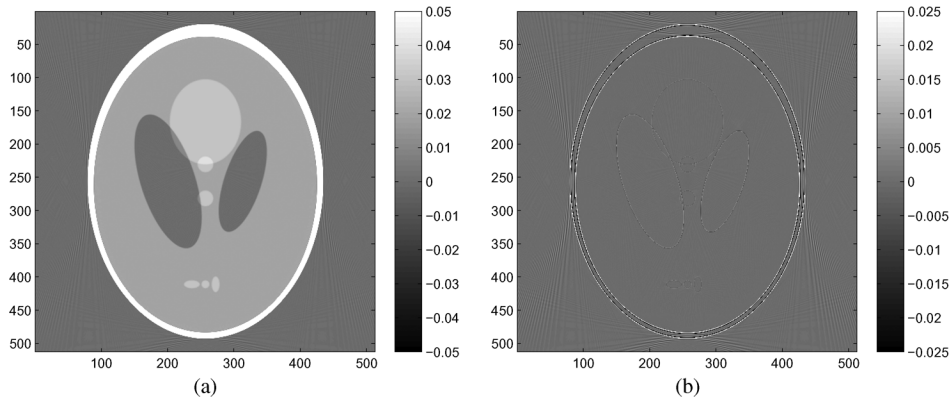


Fig. 5. Reconstruction from \tilde{P}_H^σ and \tilde{P}_V^σ . (a) Recovered Shepp-Logan. (b) Reconstruction error.

displayed in Fig. 5. Aliasing artifacts are significantly reduced, as compared with Fig. 4.

The reconstruction error is visualized by providing binary mask images where a pixel has a white color whenever the absolute reconstruction error is bigger than 1 HU for Fig. 6(a), 5 HU for Fig. 6(b), 10 HU for Fig. 6(c), and 20 HU for Fig. 6(d).

As can be seen from the images, the reconstruction error is concentrated near and outside the two external ellipses. Internal structures are reconstructed perfectly except of smoothing caused by the nonzero aperture size. Remaining aliasing artifacts are below 10 HU except of some isolated points.

We further demonstrate that the remaining artifacts are indeed aliasing results rather than reconstruction errors of our algorithm. To show this, we use reconstruction from projections that were convolved with the Gaussian function $G(x) = (1/\sigma\sqrt{\pi}) \exp(-x^2/\sigma^2)$, which has approximately the same smoothing effect on edges as the rectangular function $\Pi(x)$ but has a more compact representation in the frequency domain.

The reconstruction error for $n = 512$ and $\sigma = 2/n$ is displayed in Fig. 7(a) using a window width of 50 HU. The binary mask from the errors above 0.005 is displayed in Fig. 7(b). We observe that the reconstruction error is less than 5 HU everywhere except in the ellipse edges. The error near the edges is a result from smoothing the projections with the aperture function.

Overall, we demonstrated that our algorithm produces good reconstruction quality whenever projections are correctly sampled.

IV. FAN-BEAM RECONSTRUCTION

In Section III, we showed that the 2-D inverse DRT can be used for the reconstruction of an object from its continuous projections along lines from \tilde{S}_H and \tilde{S}_V .

Collecting this set of projections by a single pair of source/detector is a time-consuming operation since, for each projection angle, the source/detector pair should scan linearly over the orthogonal direction, collecting $2n + 1$ line integrals. This process should be repeated for each projection angle. Overall, the source should be turned on and off $2(n + 1)(2n + 1)$ times in order to collect the required projections.

In this section, we show that, if we can afford using multiple detectors with a single radiation source (as is the case with contemporary scanners), we can efficiently collect all the required line projections using certain fan-beam projections. The process, which composes parallel projections from lines that were collected using fan-beam projections, is usually referred to as “resorting.”

A. Acquisition Geometry

We consider a 2-D object, which is described by $f(x, y)$, such that $f(x, y) = 0$ outside $[-1, 1] \times [-1, 1]$. For $n = 4$, we draw all the lines from \tilde{S}_H in Fig. 8. All the line integrals in this figure can be collected using fan-beam projections with sources on the line $x = -2$. This is true for any n . Indeed, the y -coordinates of points of intersection of lines from \tilde{S}_H with the vertical line $x = -2$ are $y = -(4l/n) + (2/n)t$, which are multiples of $2/n$ by an integer from $[-2n : 2n]$.

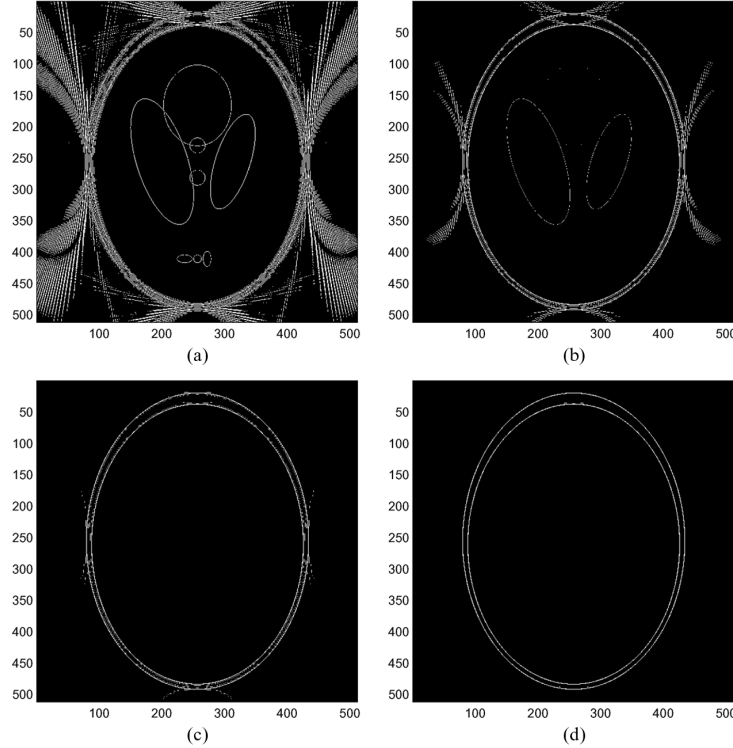


Fig. 6. Error masks from the reconstruction from \tilde{P}_H^σ and \tilde{P}_V^σ . (a) Errors above 0.001. (b) Errors above 0.005. (c) Errors above 0.01. (d) Errors above 0.02.

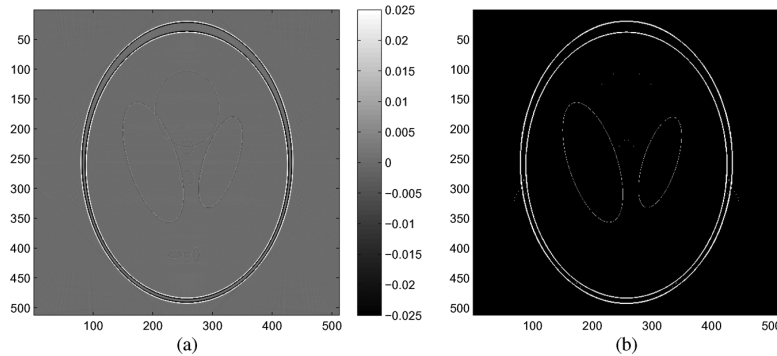


Fig. 7. Reconstruction errors from projections smoothed with a Gaussian. (a) Reconstruction error. (b) Errors above 0.005.

The points of intersection between the basically horizontal lines and the vertical line $x = 2$ are $y = 4l/n + (2/n)t$, which are also multiples of $2/n$ by an integer from $[-2n : 2n]$. Therefore, each line from \tilde{S}_H can be uniquely defined as the line that passes through the two points $(-2, (2/n)z)$ and $(2, (2/n)w)$, where $z, w \in [-2n : 2n]$.

By placing the set of detectors at the points $(2, (2/n)w)$, where $w \in [-2n : 2n]$, and by successively placing the radiation source at the points $(-2, (2/n)z)$, where $z \in [-2n : 2n]$, we can collect all the projections from \tilde{S}_H . By swapping axes, we can collect in the same way the projections along lines from \tilde{S}_V . Therefore, all the line projections required in order to reconstruct an $n \times n$ discrete approximation of $f(x, y)$ using the 2-D inverse DRT are contained in $(4n+1) + (4n+1) = 8n+2$ fan-beam projections, where the radiation source moves along a straight line with equal steps.

As we mentioned above, each line in \tilde{S}_H can be described either by the parameters (l, t) , where $l \in [-n/2 : n/2]$ and

$t \in [-n : n]$, or by the pair (z, w) , where $z, w \in [-2n : 2n]$. In Section IV-B, we establish the correspondence between these two representations.

B. The Resorting Algorithm

Consider a point $(-2, (2/n)z)$, $z \in [-2n : 2n]$. We want to find which lines from \tilde{S}_H pass through this point. Formally, for each $z \in [-2n : 2n]$, we want to find the following set:

$$S_z = \left\{ (l, t) \mid \frac{2}{n}z = \frac{2l}{n}(-2) + \frac{2}{n}t, l \in \left[-\frac{n}{2} : \frac{n}{2}\right], t \in [-n : n] \right\}.$$

We get

$$S_z = \left\{ (l, t) \mid z = -2l + t, l \in \left[-\frac{n}{2} : \frac{n}{2}\right], t \in [-n : n] \right\}.$$

If we consider a plane with Cartesian coordinates l and z , then $z = -2l + t$ is a straight line with slope -2 that intersects the

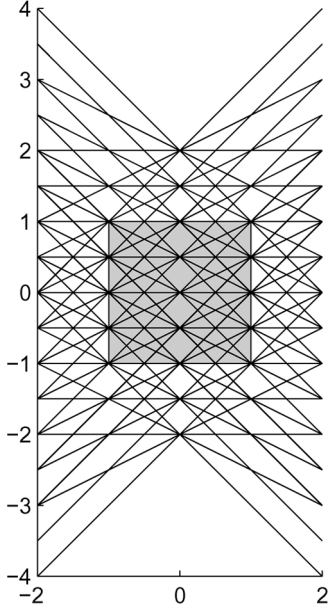


Fig. 8. Basically horizontal lines for $n = 4$.

z -axis at t . For $l \in [-n/2, n/2]$ and $t \in [-n, n]$, the points (l, z) cover a parallelogram with vertices at $(-n/2, 2n)$, $(-n/2, 0)$, $(n/2, 0)$, and $(n/2, -2n)$.

Therefore, for each $z \in [0, 2n]$, there exists $t \in [-n, n]$ such that $z = -2l + t$ if and only if $l \in [-n/2, (n-z)/2]$. Similarly, for each $z \in [-2n, 0]$, there exists $t \in [-n, n]$ such that $z = -2l + t$ if and only if $l \in [-(n+z)/2, n/2]$.

We now return to the task of finding S_z . We consider four cases, depending on whether z is even or odd and whether z is positive or negative.

Theorem IV.1: For $z \in [-2n : 2n]$, the set S_z is given by the following formulas:

- 1) For $z = 2k$, where $k \in [0 : n]$

$$S_z = \left\{ (l, z + 2l) \mid l \in \left[-\frac{n}{2} : \frac{(n-z)}{2} \right] \right\}.$$

- 2) For $z = 2k - 1$, where $k \in [1 : n]$

$$S_z = \left\{ (l, z + 2l) \mid l \in \left[-\frac{n}{2} : \frac{n-z-1}{2} \right] \right\}.$$

- 3) For $z = -2k$, where $k \in [1 : n]$

$$S_z = \left\{ (l, z + 2l) \mid l \in \left[\frac{-n-z}{2} : \frac{n}{2} \right] \right\}.$$

- 4) For $z = -2k + 1$, where $k \in [1 : n]$

$$S_z = \left\{ (l, z + 2l) \mid l \in \left[\frac{-n-z+1}{2} : \frac{n}{2} \right] \right\}.$$

Proof: We prove the case $z = 2k - 1$, where $k \in [1 : n]$. It follows from the geometric considerations above that there exists $t \in [-n, n]$ such that $z = -2l + t$ if and only if $l \in [-n/2, (n-z)/2]$, i.e., $l \in [-n/2, n/2 - k + 1/2]$. Since we are looking for integer l , this is equivalent to $l \in [-n/2 : n/2 - k]$ which is, in turn, equivalent to $l \in [-n/2 : (n-z-1)/2]$.

Since $z = -2l + t$, we have $t = z + 2l$. Consequently, $S_z = \{(l, z + 2l) \mid l \in [-n/2 : (n-z-1)/2]\}$. The proofs of the other cases are similar. ■

Corollary IV.2: A pair (z, w) defines a line from \tilde{S}_H if and only if $z, w \in [-2n : 2n]$ and $w = z + 4l$ for some $l \in S_L(z)$, where $S_L(z)$ is defined as follows:

- 1) If $z = 2k$, where $k \in [0 : n]$, then $S_L(z) = [-n/2 : (n-z)/2]$.
- 2) If $z = 2k - 1$, where $k \in [1 : n]$, then $S_L(z) = [-n/2 : (n-z-1)/2]$.
- 3) If $z = -2k$, where $k \in [1 : n]$, then $S_L(z) = [(-n-z)/2 : n/2]$.
- 4) If $z = -2k + 1$, where $k \in [1 : n]$, then $S_L(z) = [(-n-z+1)/2 : n/2]$.

Proof: It follows immediately from Theorem IV.1 and the fact that (z, w) defines some line from \tilde{S}_H if and only if there exist $l \in [-n/2, n/2]$ and $t \in [-n, n]$ such that $z = -2l + t$ and $w = 2l + t$. ■

For each pair (l, t) that defines a line from \tilde{S}_H , we can find $((2/n)z, (2/n)w)$ as the points of intersection of this line with the vertical lines $x = -2$ and $x = 2$. Therefore

$$\frac{2}{n}z = \frac{2l}{n}(-2) + \frac{2}{n}t$$

and

$$\frac{2}{n}w = \frac{2l}{n}(2) + \frac{2}{n}t$$

which is equivalent to $z = -2l + t$ and $w = 2l + t$.

Vice versa, if a pair (z, w) defines a line from \tilde{S}_H (which we can check using corollary 4.2), then the parameters (l, t) are

$$t = \frac{w+z}{2} \quad l = \frac{w-z}{4}.$$

We now describe the algorithm for collecting the set of line projections $\tilde{P}_H(t, l)$ using fan-beam projections. As usual, we assume that the object under consideration fits within the box $[-1, 1] \times [-1, 1]$. Detectors are placed at the points $(2, (2/n)w)$, where $w \in [-2n : 2n]$. Each fan-beam projection is acquired by placing the radiation source at one of the points $(-2, (2/n)z)$, where $z \in [-2n : 2n]$. We denote by $P_z(w)$ the output of the detector located at $(2, (2/n)w)$ when the object is illuminated by the point source located at $(-2, (2/n)z)$. For a fixed $z \in [-2n : 2n]$, we set $\tilde{P}_H((w+z)/2, (w-z)/4) = P_z(w)$ for all $w \in \{z + 4ll \mid l \in S_z(l)\}$. The algorithm that collects \tilde{P}_V is identical up to a swap of the axes.

It is important to notice here that we have a choice of either collecting data for all pairs (z, w) and then selecting the pairs that correspond to lines from \tilde{S}_H or collecting only the necessary projections by discarding the output of detectors for which the line given by (z, w) is not within \tilde{S}_H .

Once all the necessary projections are collected, we can reconstruct the object using the algorithm of Section III.

V. CONCLUSION

In this paper, we have shown that the inverse DRT can be used for the reconstruction of a 2-D object from its continuous projections. The DRT and its inverse are shown to model accurately the continuum as the number of samples increases. Numerical results for the reconstruction from parallel projections are presented. We also show that the inverse DRT can be used

for reconstruction from fan-beam projections with equispaced detectors.

The Shepp–Logan phantom is not a Lipschitz function, and its analytic projections are not bandlimited. Therefore, it violates the conditions of Theorem II.2. Nonetheless, the discrete projections of the phantom closely approximate the sampled continuous ones, as was shown in the paper.

CT reconstruction from parallel and fan-beam projections for 3-D X-Ray data is a natural extension of the 2-D case.

REFERENCES

[1] S. R. Deans, *The Radon Transform and Some of Its Applications*. New York: Wiley, 1983.

[2] F. Natterer, *The Mathematics of Computerized Tomography*. New York: Wiley, 1986.

[3] A. Kak and M. Slaney, *Principles of Computerized Tomographic Imaging*. New York: IEEE Press, 1988.

[4] A. Averbuch, R. R. Coifman, D. L. Donoho, M. Israeli, and Y. Shkolnisky, "A framework for discrete integral transformations I—the pseudo-polar Fourier transform," *SIAM J. Sci. Comput.*, vol. 30, no. 2, pp. 764–784, Feb. 2008.

[5] A. Averbuch, R. R. Coifman, D. L. Donoho, M. Israeli, Y. Shkolnisky, and I. Sedelnikov, "A framework for discrete integral transformations II—the 2D discrete Radon transform," *SIAM J. Sci. Comput.*, vol. 30, no. 2, pp. 785–803, 2008.

[6] A. Brandt, J. Mann, M. Brodski, and M. Galun, "A fast and accurate multilevel inversion of the Radon transform," *SIAM J. Appl. Math.*, vol. 60, no. 2, pp. 437–462, 2000.

[7] S. Basu and Y. Bresler, " $O(N^2 \log_2 N)$ filtered backprojection reconstruction algorithm for tomography," *IEEE Trans. Image Process.*, vol. 9, no. 10, pp. 1760–1773, Oct. 2000.

[8] S. Basu and Y. Bresler, "Error analysis and performance optimization of fast hierarchical backprojection algorithms," *IEEE Trans. Image Process.*, vol. 10, no. 7, pp. 1103–1117, Jul. 2001.

[9] S. Basu and Y. Bresler, "Fast hierarchical backprojection method for imaging," U.S. Patent 6 282 257, Aug. 28, 2001.

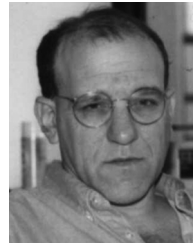
[10] J. Miao, F. Förster, and O. Levi, "Equally sloped tomography with oversampling reconstruction," *Phys. Rev. B*, vol. 72, no. 5, pp. 052 103–1–052 103–4, Aug. 2005.

[11] Y. Mao, B. P. Fahimian, S. J. Osher, and J. Miao, "Development and optimization of regularized tomographic reconstruction algorithms utilizing equally-sloped tomography," *IEEE Trans. Image Process.*, vol. 19, no. 5, pp. 1259–1268, May 2010.

[12] B. P. Fahimian, Y. Mao, P. Cloetens, and J. Miao, "Low-dose X-ray phase-contrast and absorption CT using equally sloped tomography," *Phys. Med. Biol.*, vol. 55, no. 18, pp. 5383–5400, Sep. 2010.

[13] H. Schomberg and J. Timmer, "The gridding method for image reconstruction by Fourier transformation," *IEEE Trans. Med. Imag.*, vol. 14, no. 3, pp. 596–607, Sep. 1995.

[14] F. Matus and J. Flusser, "Image representation via a finite Radon transform," *IEEE Trans. Pattern Anal. Mach. Intell.*, vol. 15, no. 10, pp. 996–1006, Oct. 1993.



Amir Averbuch was born in Tel Aviv, Israel. He received the B.Sc. and M.Sc. degrees in mathematics from The Hebrew University of Jerusalem, Jerusalem, Israel, in 1971 and 1975, respectively, and the Ph.D. degree in computer science from Columbia University, New York, NY, in 1983.

During 1966–1970 and 1973–1976, he served with the Israeli Defense Forces. In 1976–1986, he was a Research Staff Member with the Department of Computer Science, IBM T.J. Watson Research Center, Yorktown Heights, NY. In 1987, he joined

the School of Computer Science, Tel Aviv University, Tel Aviv, Israel, where he is currently a Professor of computer science. His research interests include applied harmonic analysis, wavelets, signal/image processing, numerical computation, and scientific computing.



Ilya Sedelnikov was born in Novosibirsk, Russia. He studied mathematics in Novosibirsk state university, Novosibirsk, Russia, in 1990–1993, before moving to Israel in 1993. He received the B.Sc. degree in computer science from Ben-Gurion University, Be'er Sheva, Israel, in 1997; and the M.Sc. degree in computer science from Tel Aviv University, Tel Aviv, Israel, in 2004.

He is currently an Image Processing Algorithm Engineer with the Samsung Israel Research Center.

His research interests include fast image reconstruction/processing algorithms, music signal processing, and dimensionality reduction methods for data analysis.



Yoel Shkolnisky received the B.Sc. degree in mathematics and computer science and the M.Sc. and Ph.D. degrees in computer science from Tel Aviv University, Tel Aviv, Israel, in 1996, 2001, and 2005, respectively.

From July 2005 to July 2008, he was a Gibbs Assistant Professor of applied mathematics with the Department of Mathematics, Yale University, New Haven, CT. Since October 2009, he has been with the Department of Applied Mathematics, School of Mathematical Sciences, Tel Aviv University.

His research interests include computational harmonic analysis, scientific computing, and data analysis.